Optimization of Smart Spoiler for Race Car

M.H. Djavareshkian, A. Esmaeli

Abstract— A pressure-based implicit procedure to solve Navier-Stokes equations on a nonorthogonal mesh with collocated finite volume formulation is used to simulate flow around the smart and conventional flaps of spoiler under the ground effect. Cantilever beam with uniformly varying load with roller support at the free end is considered for smart flaps. The boundedness criteria for this procedure are determined from a Normalized Variable diagram (NVD) scheme. The procedure incorporates the $k - \varepsilon$ eddy-viscosity turbulence model. The method is first validated against experimental data. Then, the algorithm is applied for turbulent aerodynamic flows around a spoiler section with smart and conventional flaps for different attack angle, flap angle and ground clearance where the results of two flaps are compared. So the best position of spoiler is achieved based on PSO optimization algorithm, so that if the spoiler put in this position, produced maximum aerodynamic forces.

Keywords— Smart spoiler, Ground Effect, Flap, Aerodynamic coefficients, Race car.

I. INTRODUCTION

The total aerodynamic package of the race car is emphasized now more than ever before. The use of aerodynamics to increase the cars' grip was pioneered in Formula one in the late 1960s by Lotus, Ferrari and Brabham. Aerodynamics plays a vital role in determining speed and acceleration and thus performance. While drag reduction is an important part of the research, down force generation plays a greater role in lap time reduction. Ground effect aerodynamics of race cars is concerned with generating down force, principally via low pressure on the surfaces nearest to the ground. These phenomena happen when a wing is going near the surface. Airfoils or wings are used in the front and rear of the car in an effort to generate more down force. The front wing of a race car is an important piece to make safety at high speed and produces about 1/3 of the car's down force, it has experienced more modifications than rear wing. The front wing assembly is the first part of the car to meet the air mass. The flow field here is better than at other parts of the car because the air here has been disturbed the least. The wing is designed to produce down force and guide the air as it moves toward the body and rear of the car. Flaps and winglets

M.H. Djavareshkian is with the Ferdowsi University of Mashhad (corresponding author to provide phone: 303-555-5555; fax: 303-555-5555; e-mail: javareshkian@Ferdowsi.um.ac.ir).

A. Esmaeli, is with the Ferdowsi University of Mashhad. He is now M.S Student in the Department of Mechanics, Ferdowsi University of Mashhad, (aliesmaeli30316@yahoo.com).

may also be used. In setting up the front wing assembly, engineers must consider what happens to the airflow as it travels toward the back of the car. Jonathan and Xin [1], studied about flap wing in ground effect for racing car application.

A general overview of the racing vehicle R&D process is studied by Daisuke et al. [2]. A CFD simulation and analysis for a 50% scaled car model is presented in sufficient detail, with an emphasis on addressing its aerodynamic aspects. Kengo and Hiroshi [3] found the optimal flap chord length with using CFD simulations in two-dimension FX63-137 airfoil. Jagadeep and Mayank [4] investigated about front wing in the race car by using CFD software and founded the optimum angle of attack for a F1 car(Formula one race). Joseph [5] investigated aerodynamic of race car and typical design tools such as wind tunnel testing, computational fluid dynamics, track testing and their relevance to race car development are discussed as well. Mokhtar [6] and [7] studied for low Reynold's number flow around wings with and without ground effect. The mention study was extended to three-dimensional flow around a wing with ground effect [7]. Mokhtar and Jonathan [8], investigated about a numerical study of a race car front wing. The focus of their study is to investigate the aerodynamics characteristics of a wing operating in a small ground clearance. A computational study in order to model the flow around an inverted airfoil in ground effect were performed by Zerihan and Zhang [9].

The knowledge of the effects that the ground can have on airfoils dates back to the early 1920's. In recent years, there have been successful investigations on the aerodynamics of airfoil and wing. One of the more recent wind tunnel experiments was done by Ahmed and Sharma [10] and [11]. Jung et al. [12], simulated three-dimensional NACA6409 in ground proximity. Smith [13] performed the computational analysis of airfoils in ground effect. Influence of endplate on aerodynamic characteristics for low-aspect-ratio wing in ground effect is performed by Park and Lee [14]. Effect of ground proximity on the aerodynamic performance and stability of a light unmanned aerial vehicle has been performed by Boschetti et al. [15]. The shape optimization using the multi-objective genetic algorithm and the analysis of the three-dimensional wings in ground effect have been performed by Lee et al. [16].

Due to the potential benefits of employing adaptive airfoil, there has been an intensive attempt by researchers in developing a working model. With the advancement of

materials, many are now considering using smart materials to produce airfoil with variable camber capability. An analytical study conducted by NASA on the benefits of variable-camber capability [17]. Another advantage of adaptive airfoil is that it causes smaller vortex with less power. This was the result of Pern and Jacob [18] research. They used piezoelectric stimulus with a steel layer in airfoil. Kudva et al. [19] discussed about smart structure technologies and their benefits. In 2003, Forster et al. [20] designed a two dimensional airfoil with a control surface in trailing edge that has a chord wise geometrical changes.

Conventional spoiler have been used in most of the researches for race cars. To improve aerodynamic coefficient performance, a smart spoiler can be used in these cars. In this research, the smart flap is employed and simulated for a spoiler section in ground clearance. In this simulation, the performance of airfoil with smart and conventional flaps for different length, flap angle and ground clearance are studied.

In all previous studies, spoilers of car were investigated from different directions but none of them achieved the best installation position of spoiler. In this study, optimization is done based on PSO algorithm so that the best of distance approximation of surface, angle of flap deflection and the best flap length is achieved based on maximum of lift to drag ratio production.

II. NUMERICAL SOLUTION SETUP AND CONDITIONS

A. Simulation smart flap deflection

In this study, a smart flap deflection is designed with a cantilever beam so that the beam bending equation is same a smart flap chord deflection. Beside a flap shape is a triangle (see e.g. Fig. 1), so the cantilever beams with uniformly varying load are considered (see e.g. Fig. 2). The mention profile is given below:

$$Y = \frac{w_0(-X^5 + 2B^2 X^3 - B^4 X)}{120 E \bar{I} B} \qquad (1)$$

Since the parametric equation only needs, equation (1) is substituted by equation (2).

$$\begin{aligned} Y_{Upper} &= Y_u + k_u(-X^5 - aX^3 + X) \\ Y_{Lower} &= Y_L + k_L(-X^5 - aX^3 + X) \end{aligned} \qquad (2)$$

$$a = \frac{1 - B^4}{B^2}$$

The bending equation can be used for midline. For upper and lower flap surface, the configuration was manipulated by making minor modifications. The coefficients of equation(2) are determined by an iterative process. Each profile is visualized using FORTRAN, and the value of the coefficient

is either increased or decreased until the desired profile is obtained. A parametric smart airfoil is designed, and computational fluid dynamics simulation is done over them.
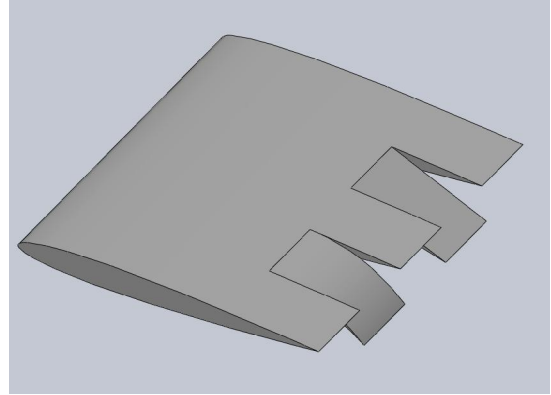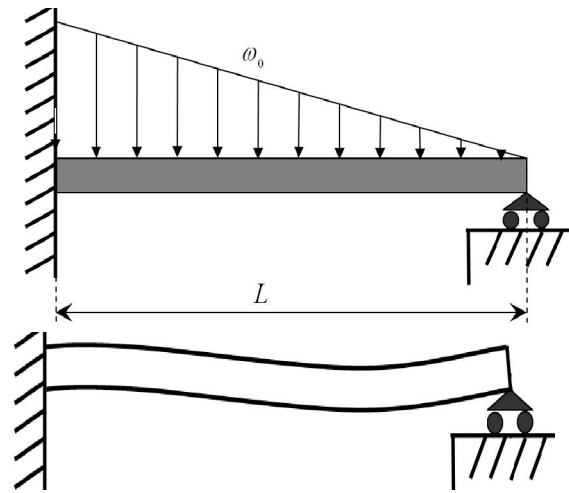

Fig. 1 Smart and Convectional Flap

Fig. 2 Cantilever beam model.

B. Governing Equation for Fluid

The basic equations, which describe conservation of mass, momentum and scalar quantities, can be expressed in the following vector form, which is independent of the coordinate system.

$$div(\rho \vec{V}) = S_m \qquad (3)$$

$$div(\rho \vec{V} \otimes \vec{V} - \vec{T}) = \vec{S}_v \qquad (4)$$

$$div(\rho \vec{V} \phi - \vec{q}) = \vec{S}_\Phi \qquad (5)$$

The latter two are usually expressed in terms of basic dependent variables. The stress tensor for a Newtonian fluid is:

$$\vec{T} = -(P + \frac{2}{3}\mu \, div \, \vec{V})\vec{I} \qquad (6)$$

and the Fourier-type law usually gives the scalar flux vector:

$$\vec{\mathbf{q}} = \Gamma_\phi \, \mathrm{grad}\Phi \qquad (7)$$

Since the $k - \varepsilon$ model is simple and has good stability with easy convergence. Besides the angle of attack is zero, the maximum angle of flap is 7.5° and there is not strong separation therefore, flow filed is not swirl and complicate. The $k - \varepsilon$ model has been chosen in this simulation.

C. Finite-Volume Discretization

The discretization of the above differential equations is carried out using a finite-volume approach. First, the solution domain is divided into a finite number of discrete volumes or cells, where all variables are stored at their geometric centers (see e.g. Fig.3). The equations are then integrated over all the control volumes by using the Gaussian theorem. The discrete expressions are presented affected concerning only one face of the control volume, namely, e for the sake of brevity. For any variable ϕ (which may also stand for the velocity components), the result of the integration yields:

$$I_e - I_w + I_n - I_s = S_\phi \, \delta \upsilon \qquad (8)$$

where I's are the combined cell-face convection I^c and diffusion I^D fluxes. The diffusion flux is approximated by central differences and can be written for cell-face e of the control volume in Fig. 3 as:

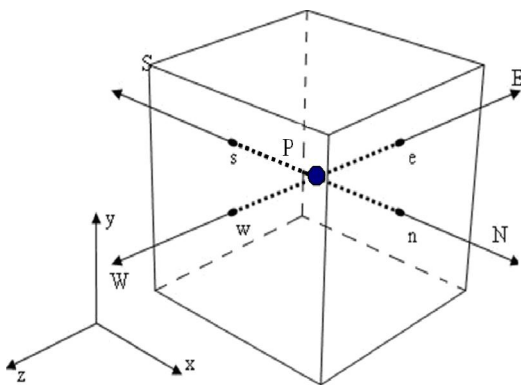$$I_e^D = D_e(\phi_P - \phi_E) \qquad (9)$$

Fig. 3 Finite volume and storage arrangement.

The discretization of the convective flux, however, requires special attention and is the subject of the various schemes developed. A representation of the convective flux for cell-face e is:

$$I_e^c = (\rho.V.\mathrm{A})_e \, \phi_e = F_e \phi_e \qquad (10)$$

The value of ϕ_e is not known and should be estimated by interpolation, from the values at neighboring grid points. The expression for the ϕ_e is determined by the SBIC scheme [21], that is based on the NVD technique, used for interpolation from the nodes E, P and W. The expression can be written as:

$$\phi_e = \phi_W + (\phi_E - \phi_W).\tilde{\phi}_e \qquad (11)$$

So that:

$$\tilde{\phi}_e = \tilde{\phi}_P \quad , \text{If} \quad \tilde{\phi}_C \notin [0,1] \qquad (12)$$

where

$$\tilde{\phi}_P = \frac{\phi_P - \phi_W}{\phi_E - \phi_W}, \qquad \tilde{\phi}_e = \frac{\phi_e - \phi_W}{\phi_E - \phi_W}$$

$$\tilde{x}_P = \frac{x_P - x_W}{x_E - x_W}, \qquad \tilde{x}_e = \frac{x_e - x_W}{x_E - x_W} \qquad (13)$$

The limits on the selection of K could be determined in the following way. Obviously, the lower limit is $K = 0$, which would represent switching between upwind and central differencing. This is not favorable because, it is essential to avoid the abrupt switching between the schemes in order to achieve the converged solution. The value of K should be kept as low as possible in order to achieve the maximum resolution of the scheme.

The final form of the discretized equation from each approximation is given as:

$$A_P.\varphi_P = \sum_{m=E,W,N,S} A_m.\varphi_m + S'_\varphi \qquad (14)$$

The results are presented and discussed in the next section. At the first, grid setup and computational domain has been described.

D. Grid Strategy

The grid structure that used in CFD simulation was created by a structured mesh employed because of its simplicity and applicability to the current flow configuration (i.e., with a near-by ground). Schematic shape of these two-dimensional structured grids is shown in Fig. 4.
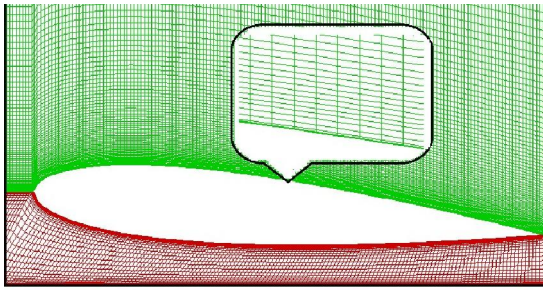
Fig. 4 grid topology and H grid.

According to Fig. 5 the dimension of domain has been obtained after doing several various lengths for b, f, u and independent lengths have been chosen. The grid sizing was determined after grid independence that was found by doing several different trials, which show for surface pressure coefficient distribution. For example, the effect of grid size is shown in Fig. 6. For other cases, the above process is used for grid and domain independences.
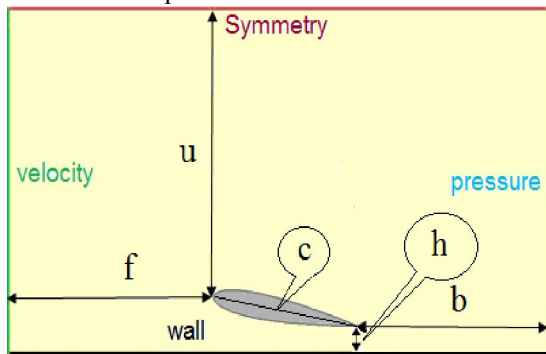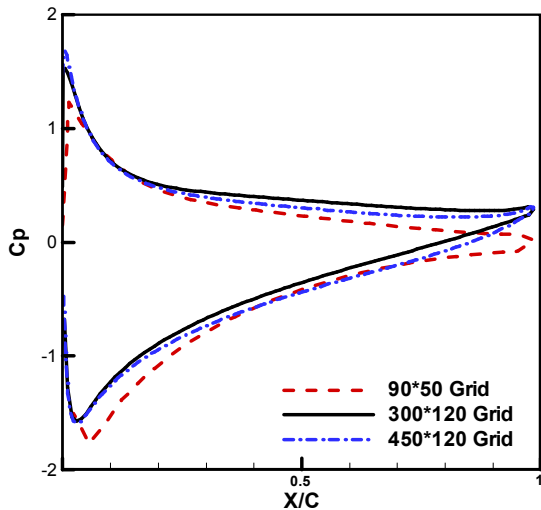

Fig. 5 Dimension of domain.

Fig. 6 Effect of grid sizing on pressure distribution on the surface of the airfoil for an angle of attack 10° and h/c=0.2.

E. Boundary Conditions

Fig. 5 shows the boundary condition. At the inlet, velocity has been prescribed. At the outlet, the pressure is fixed. Slip boundary conditions are used on upper walls of the domain and wall boundary conditions are used for airfoil surface and ground surface.

III. PARTICLE SWARM OPTIMIZATION (PSO)

PSO is a robust stochastic optimization technique based on the movement and intelligence of swarms. PSO applies the concept of social interaction to problem solving. It was developed in 1995 by James Kennedy (social-psychologist) and Russell Eberhart (electrical engineer). It uses a number of agents (particles) that constitute a swarm moving around in the search space looking for the best solution. Each particle is treated as a point in a N-dimensional space which adjusts its flying according to its own flying experience as well as the flying experience of other particles. Each particle keeps track of its coordinates in the solution space which are associated with the best solution (fitness) that has achieved so far by that particle. This value is called personal best, pbest. Another best value that is tracked by the PSO is the best value obtained so far by any particle in the neighborhood of that particle. This value is called gbest.

The basic concept of PSO lies in accelerating each particle toward its pbest and the gbest locations, with a random weighted acceleration at each time step as shown in Fig. 7.
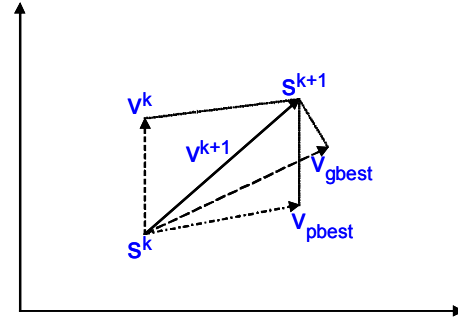

Fig.7 Concept of modification of a searching point by PSO

Each particle tries to modify its position using the following information: the current positions, the current velocities, the distance between the current position and pbest, the distance between the current position and the gbest. The modification of the particle's position can be mathematically modeled according the following equation:

$$V_i^{k+1} = \omega V_i^k + c_1 rand_1(...)x(pbest_i - s_i^k) +$$
$$c_2 rand_2(...)x(gbest - s_i^k).....\tag{15}$$

Rand is uniformly distributed random number between 0 and 1. $pbest_i$ is the personal best of agent i, and gbest is global best of the particle group.

The following weighting function(**w**) is usually utilized in (15):

$$\omega = w_{Max} - [(w_{Max} - w_{Min})x iter]/\max iter \tag{16}$$

where w_{Max} is initial weight, w_{Min} is final weight, maxIter is maximum iteration number, and iter is current iteration number.

$$s_i^{k+1} = s_i^k + V_i^{k+1} \qquad (17)$$

IV. RESULTS AND DISCUSSION

The results are presented and discussed in this section. Table I shows the setting for numerical simulation. At the first, simulation of flow around the airfoil NACA0015 has been performed. Then, the effects of flow around airfoil NACA0009 with flap in smart and conventional conditions, angle of flap and ground clearance have been investigated. The simulation is two-dimensional. Pressure coefficient distribution, Lift and drag coefficients of the airfoil have been analyzed. The Reynolds number for this study is 2.4×10^5. This number indicates that the airflow has both laminar and turbulent regions.

TABLE I
SETTINGS FOR NUMERICAL SIMULATION

Flow	turbulent
Precision	Two-dimension Double Precision
Scheme	Normalize variable diagram
Solver	SIMPLE
turbulent model	$k-\varepsilon$

The numerical and experimental pressure coefficient distributions on the surface of the airfoil for angles of attack 7.5° and ground clearance h/c=0.8 are compared in Fig. 8. It can be seen that there is good agreement between present numerical and experimental data [11]. Table II also shows lift coefficients and error percent. The numerical results are in good agreement with experiment data.
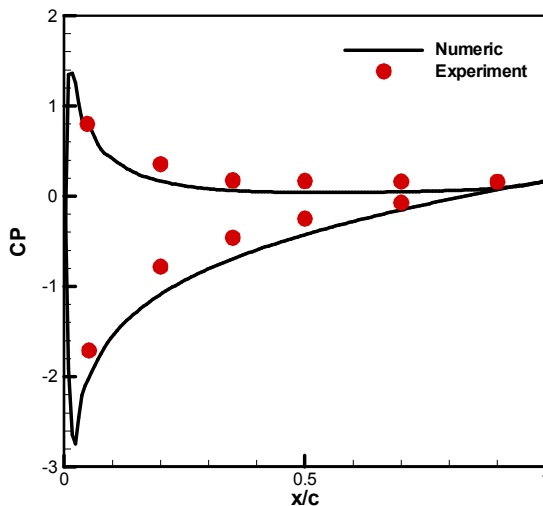

Fig. 8 Pressure coefficient distribution on the surface of the airfoil NACA 0015 for an AOA 7.5° and h/c=0.8.

The airfoil which was selected to be used in this study is the NACA0009. The simulation method for this test case is the same of pervious test. Airflow treatment and effect of the flap in smart and conventional conditions in ground

proximity are investigated.

TABLE II
COMPARISON OF LIFT COEFFICIENTS FOR AIRFOIL NACA 0015 AND AOA= 7.5°.

h/c	Experiment	Numeric	Error%
0.1	0.983	0.855	13
0.5	0.845	0.756	10
0.8	0.779	0.735	6

Fig. 9 and 10, respectively, show the pressure coefficient distribution on the surface of smart and conventional airfoils for AOF= +5° and different ground clearance. When the flap deflected to upward, pressure side is related to the upper surface of airfoil and suction side is related to the lower surface of airfoil. As figures show pressure is reduced with decreasing ground clearance in the pressure side. This behavior happens in both smart and conventional flaps.
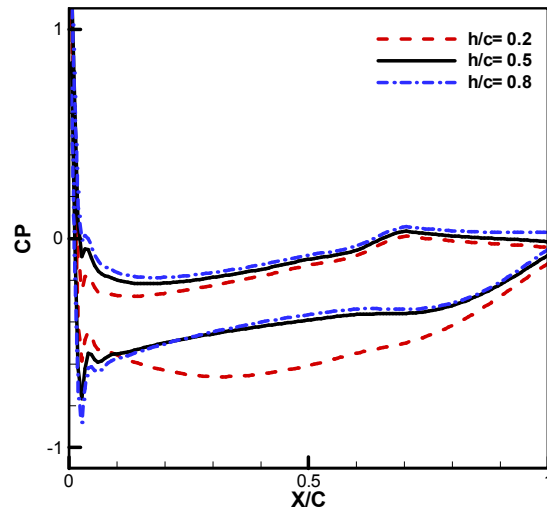

Fig. 9 Pressure coefficient distribution on the surface of the smart airfoil for AOF= +5°.

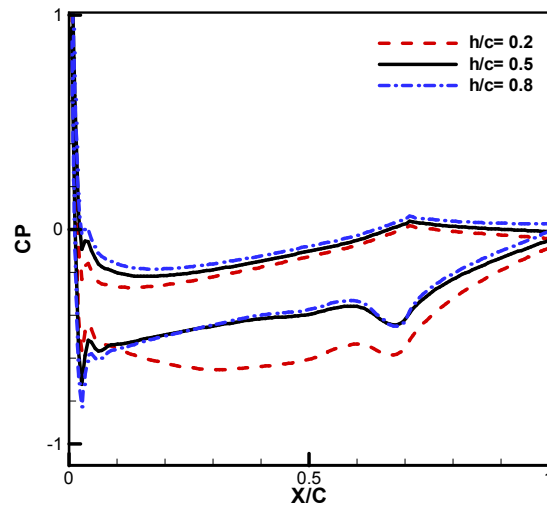Fig. 10 Pressure coefficient distribution on the surface of the conventional airfoil for AOF= +5°.

Table III shows down force(Lift) and drag coefficients and

L/D for smart and conventional flaps. Comparisons show that down force coefficients of smart flaps increase and their drag coefficients decrease as results L/D ratio for smart flaps are higher than conventional flaps.

TABLE III
DOWN FORCE(LIFT) (A) AND DRAG (B) COEFFICIENTS AND LIFT - DRAG RATIO(C) FOR SMART AND CONVENTIONAL AIRFOILS FOR AOF= +5°.

h/c	Smart Flap	Convection Flap
0.2	-0.385	-0.368
0.5	-0.309	-0.288
0.8	-0.337	-0.308

(a)

h/c	Smart Flap	Convection Flap
0.2	0.0382	0.0386
0.5	0.0295	0.0305
0.8	0.0270	0.0276

(b)

h/c	Smart Flap	Convection Flap
0.2	10.1	9.53
0.5	10.5	9.44
0.8	12.5	11.2

(c)

Table VI shows down force(Lift), and Drag coefficients and L/D for smart and conventional airfoils for h/c=0.8. Comparisons show that down force coefficient of a smart flap is more than a conventional flap. Down force and drag coefficients increase slightly with angle of flap for two airfoils.

TABLE VI
DOWN FORCE (LIFT) (A) AND DRAG (B) COEFFICIENT AND LIFT - DRAG RATIO(C) FOR SMART AND CONVENTIONAL AIRFOILS FOR H/C=0.8.

AOF (deg)	Smart Flap	Convection Flap
+2.5	-0.160	-0.141
+5	-0.337	-0.308
+7.5	-0.522	-0.475

(a)

AOF (deg)	Smart Flap	Convection Flap
+2.5	0.0259	0.0268
+5	0.0270	0.0276
+7.5	0.0278	0.0290

(b)

AOF (deg)	Smart Flap	Convection Flap
+2.5	6.18	5.26
+5	12.5	11.2
+7.5	18.8	16.4

(c)

Fig. 11 and 12 show lift and drag coefficients for the different h/c. Fig. 11 shows that drag coefficient increases with reduction ground clearance and this coefficient for conventional flaps is more than the smart mode for all the h/c and AOF.
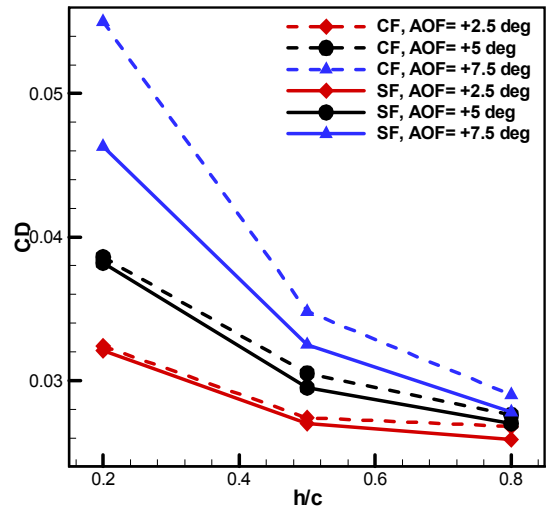

Fig. 11 Variations in CD as a function of h/c for smart and conventional flap and different angle of flap.

Fig. 12 indicates lift coefficient increases with ground clearance initially, then this coefficient decreases with increasing ground clearance. The positive deflection of flap passes flow between the lower surface of airfoil and ground surface like flow passing a nozzle. Nozzle Characteristics revealed that velocity increases and pressure reduces in the convergent part so velocity reaches maximum in the gorge and pressure increase and velocity decrease in the divergent part. When the ground clearance is reduced, the cross section ratio is greater and flow expansion is more on the lower surface of airfoil. As a result, velocity on the lower surface of airfoil increases. This increase of velocity in the lower surface with ground clearance from h / c = 0.8 to h / c = 0.5 increases lift coefficient. When the ground clearance decreases from h/c=0.5 to h/c=0.2, boundary layer has an important role, the velocity in lower surface and lift coefficient decrease. Fig. 13 shows the L/D absolute value ratio for the different h/c.
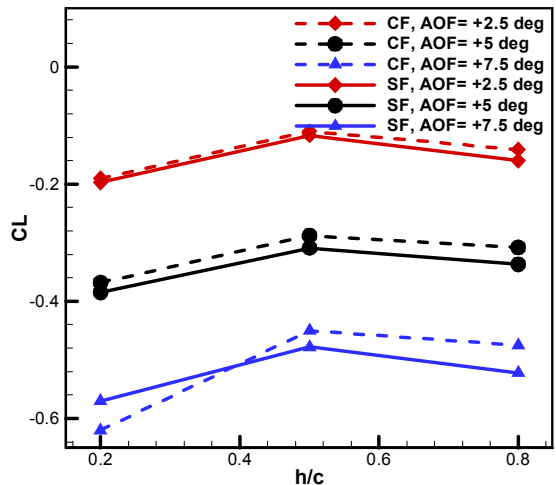

Fig. 12 Variations in CL as a function of h/c for smart and conventional flap and different angle of flap.
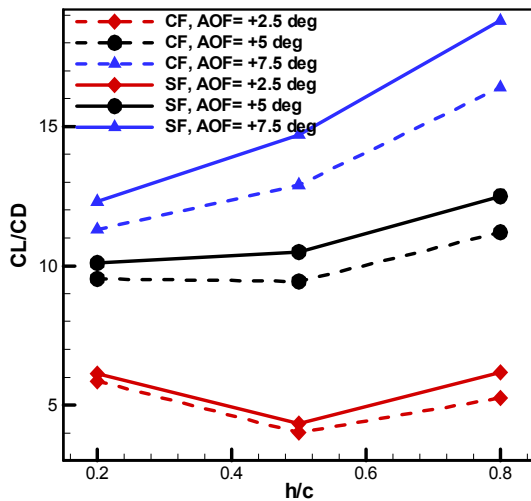
Fig. 13 Variations in L/D as a function of h/c for smart and conventional flap and different angle of flap.

TABLE V
VOLUME FLOW RATE PASSING BETWEEN LOWER SURFACE OF AIRFOIL AND GROUND FOR H/C=0.2.

AOF(deg)	Smart Flap	Conventional Flap
+7.5°	0.631	0.643
+5°	0.600	0.594
+2.5°	0.568	0.567

So far effect of angle of flap deflection, distance approximation from the car surface and flap length has been investigated. The results show that if used smart flap, the aerodynamic performance of spoiler is increased. But to get the best optimal mode is important. Therefore, optimization has been done based on PSO algorithm. Fig. 14 shows variations in absolute of lift to drag ratio as a function of flap length and angle of flap. This figure shows that the absolute of lift to drag ratio is increased with increasing angle of flap and flap length.
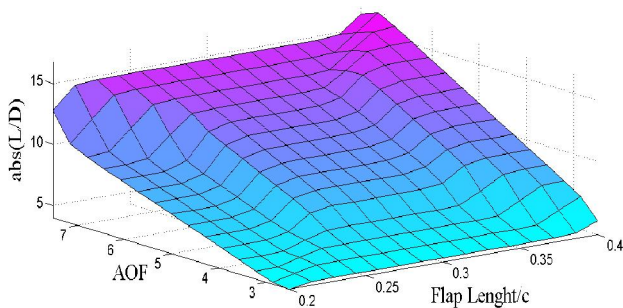

Fig. 14 Variations in absolute of L/D as a function of flap length and angle of smart flap.

Fig. 15 shows variations in absolute of lift to drag ratio as a function of h/c and angle of flap. This figure shows that the absolute of lift to drag ratio is inceased with increasing the distance approximation. Fig. 16 shows variations in absolute of lift to drag ratio as a function of flap angle and flap length. This figure shows that the absolute of lift to drag ratio is increased with increasing flap length and h/c.
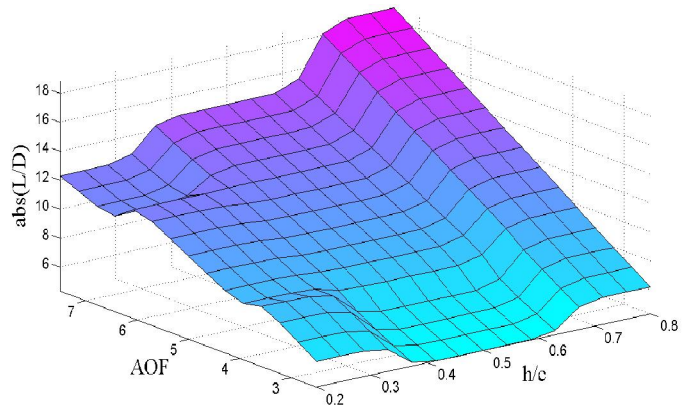

Fig. 15 Variations in absolute of L/D as a function of h/c and angle of smart flap.
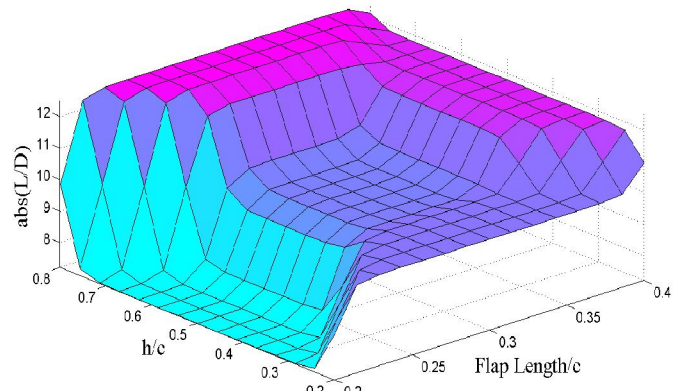

Fig. 16 Variations in absolute of L/D as a function of h/c and flap length for smart flap.

So optimization is done with the present results. Initially absolute of lift to drag ratio is obtained as a function of flap length(FL/c), flap angle(AOF) and distance approximation from the surface by using neural network-fuzzy and ultimately optimization is performed based on L/D=f(FL/c, h/c, AOF). According to the available data optimization mode is obtained in table VI.

TABLE VI
OPTIMIZATION CASE FOR SMART FLAP

AOF(deg)	h/c	FL/c	Abs(L/D)
+7.47°	0.78	0.28	18.74

While flap length to chord ratio will be 0.28, angle of flap deflection is 7.47° and spoiler distance from surface is 0.78 then produced maximum of aerodynamic performance and absolute of lift to drag ratio is 18.74 and this case suggested for the optimal case for installation of spoiler on the car.

V. CONCLUTION

A pressure-based implicit procedure to solve Navier-Stokes equations on a non-orthogonal mesh with collocated finite volume formulation is used to simulate flow around the smart and conventional flaps of a spoiler section under the ground effect. The algorithm is applied for different flap length, flap

angle and ground clearance. The main findings can be summarized as follows: 1-The agreement between presented predation and experimental data is considerable 2-The pressure coefficient distribution in a smart flap is smoother than conventional flap 3- Lift-drag ratio in a smart flap is higher than a conventional flap 4- The highest lift-drag ratio is at flap angle 7.5º 5- The ground clearance with h/c=0.5 has the highest lift coefficient 6- The lift and drag coefficients slightly increase for longer flap length and L/D ratio increases too 7- The optimal mode is obtained based on PSO algorithm.

NOMENCLATURE

h	=	Ground Clearances
AOA	=	Angle of Attack
A	=	Cell Face Area
μ	=	Dynamic Viscosity
$\tilde{\phi}$	=	Normalized Scalar Quantity
K	=	a factor in SBIC scheme to determine a special scheme
ω_0	=	Weight/Unit Length(N/m)
$\overline{I}$	=	Area moment of inertia(m^4)
B	=	Length of the Beam
X	=	Horizontal Cartesian Coordinate
Y	=	Vertical Cartesian Coordinate
E	=	Young's Modulus
ρ	=	Density
P	=	Pressure
Γ	=	Diffusivity Coefficient
$\bar{q}$	=	Scalar Flux Vector
F	=	Mass Flux
$\vec{T}$	=	Stress Tensor
$\delta\upsilon$	=	Cell Volume
$\vec{S}$	=	Source Term
$\vec{V}$	=	Velocity Vector
ϕ	=	Scalar Quantity
I	=	Flux
S_k	=	Current Searching Point
S_{k+1}	=	Modified Searching Point
V_k	=	Current Velocity
V_{k+1}	=	Modified Velocity
V_{pbest}	=	Velocity based on pbest
V_{gbest}	=	Velocity based on gbest
v_i^k	=	Velocity of agent i at Iteration k
c_j	=	Weighting Factor
s_i^k	=	Current Position of agent i at Iteration k

REFERENCES

[1] J. Zerihan and X. Zhang, "Aerodynamics of Gurney Flaps on a Wing in Ground Effect," *AIAA journal,* vol. 39, pp. 772-780, 2001.

[2] D. Ueno, G. Hu, I. Komada, K. Otaki, and Q. Fan, "CFD Analysis in Research and Development of Racing Car," presented at the Motorsports Engineering Conference & Exposition, Dearborn, MI, USA, 2006.

[3] K. Goto and H. Sakurai, "Numerical Study for the Optimal Flap Chord Length of a Two-Element Airfoil," *SAE International Journal of Passenger Cars-Mechanical Systems,* pp. 1-3643, 2006.

[4] J. Reddy and M. Gupta, "Finding the Optimum Angle of Attack for the Front Wing of an F1 Car Using CFD," in *4th WSEAS International Conference on Fluid Mechanics and Aerodynamics*, Elounda, Greece, 2006, pp. 29-34.

[5] J. Katz, "Aerodynamics of Race Cars," *Annual Review of Fluid Mechanics,* vol. 38, p. 27, 2005.

[6] W. Mokhtar, "A Numerical Study of High-Lift Single Element Airfoils with Ground Effect for Racing Cars," *SAE transactions,* vol. 114, pp. 682-688, 2005.

[7] W. Mokhtar, "Aerodynamics of High-Lift Wings with Ground Effect for Racecars," presented at the SAE World Congress, 2008.

[8] W. Mokhtar and J. Lane, "Racecar Front Wing Aerodynamics," *SAE International Journal of Passenger Cars-Mechanical Systems,* vol. 1, p. 1392, 2009.

[9] J. Zerihan and Z. Xin, "Aerodynamics of a Single Element Wing in Ground Effect," *Journal of aircraft,* vol. 37, pp. 1058-1064, 2000.

[10] M. Ahmed, S. H. Ali, G. M. Imran, and S. D. Sharma, "Experimental Investigation of the Flow Field of a Symmetrical Airfoil in Ground Effect," in *21st Applied Aerodynamics Conference*, Orlando, Florida, 2003.

[11] M. Ahmed and S. Sharma, "An Investigation on the Aerodynamics of a Symmetrical Airfoil in Ground Effect," *Experimental Thermal and Fluid Science,* vol. 29, pp. 633-647, 2005.

[12] K. Jung, H. Chun, and H. Kim, "Experimental Investigation of Wing-in-Ground Effect with a NACA6409 Section," *Journal of marine science and technology,* vol. 13, pp. 317-327, 2008.

[13] J. Smith, "Computational Analysis of Airfoils in Ground Effect for Use as a Design Tool," M.Sc Mechanical and Aerospace Engineering Department, West Virginia University, West Virginia, 2007.

[14] K. Park and J. Lee, "Influence of Endplate on Aerodynamic Characteristics of Low-Aspect-Ratio Wing in Ground Effect," *Journal of mechanical science and technology,* vol. 22, pp. 2578-2589, 2008.

[15] J. P. Boschetti, M. E. Cárdenas, and A. AmerioCLq, "Stability and Performance of a Light Unmanned Airplane in Ground Effect," in *48th AIAA Aerospace Sciences Meeting Including the New Horizons Forum and Aerospace Exposition*, Florida, 2010.

[16] J. Lee, C. Hong, B. Kim, K. Park, and J. Ahn, "Optimization of Wings in Ground Effect Using Multi-Objective Genetic Algorithm," in *48th AIAA Aerospace Sciences Meeting Including the New Horizons Forum and Aerospace Exposition*, Florida, 2010.

[17] A. Bolonkin, G. Gilyard, H. L. D. F. R. Center, U. S. N. Aeronautics, and S. Administration, *Estimated benefits of variable-geometry wing camber control for transport aircraft*: Citeseer, 1999.

[18] N. J. Pern and J. D. Jacob, "Wake Vortex Mitigation using Adaptive Airfoils," presented at the 37th AIAA. Aerospace Sciences Meeting and Exhibit, 1999.

[19] J. Kudva, C. Martin, A. Jardine, G. Sendeckyj, T. Harris, A. McGowan, and R. Lake, "Design, Fabrication, and Testing of the DARPA/Wright Lab" Smart Wing" Wind Tunnel Model," *Journal of American Institute of Aeronautics and Astronautics (AIAA),* 1997.

[20] E. Forster, B. Sanders, and F. Eastep, "Synthesis of a Variable Geometry Trailing Edge Control Surface," *AIAA paper,* vol. 1717, 2003.

[21] M. Djavareshkian, "A new NVD Scheme in Pressure-Based Finite-Volume Methods," in *14th Australasian Fluid Mechanics conference*, , Adelaide University, Adelaide, Australia, 2001, pp. 10-14.